Automatic Detection of Local Cloud Systems from MODIS Data

G. CAPPELLUTI, A. MOREA, C. NOTARNICOLA, AND F. POSA

Dipartimento Interateneo di Fisica, Università degli Studi di Bari, and Politecnico di Bari, Bari, Italy

(Manuscript received 11 January 2005, in final form 19 September 2005)

ABSTRACT

This paper describes an algorithm that is aimed at the identification of cloudy and clear pixels in Moderate-Resolution Imaging Spectroradiometer (MODIS) images to support earth science and nowcasting applications. The process from geolocated and calibrated data allows one to obtain cloud masks with four clear-sky confidence levels for five different cloud system types. The technique has been developed using the MODIS cloud-mask algorithm heritage, but the threshold tests performed have been executed without comparing solar reflectances and thermal brightness temperatures with thresholds determined in advance, but instead with thresholds carried out from classification methods. The main advantage of this technique is that the thresholds are obtained directly from the images. Seventy-five percent of the spectral signatures (known as end members) derived from the winter images in the detection of the various cloud types and 80% of the summer end members can be considered as being well discriminated. Furthermore, it seems that the end members characterizing the different cloud systems are constant throughout the various seasons of the year (they vary with a confidence level of 60%), whereas those describing clear sky change in a notable manner (the associated confidence level is 99%). The algorithm is able to produce cloud masks pertinent to limited regions at a mesoscale level, which may be a key factor for nowcasting purposes. This work shows that the use of end members and spectral angles, as opposed to spectral thresholds, should be carefully examined because of the fact that it might be simpler or that higher performances may be achieved at a regional scale.

1. Introduction

Clouds reflect a considerable amount of incoming solar energy back to space before it can be absorbed by the earth's system, thus cooling the terrestrial surface. At the same time, they absorb a large amount of the outgoing infrared radiation, thus inhibiting the earth's system from releasing heat back into space and henceforth warming the atmosphere. Whether the surface of the earth will heat or cool depends on several factors, including cloud altitude and size as well as the makeup of the particles that form the cloud. Cloud cover plays a key role in the radiative balance of the earth and must be accurately described to assess weather and climatic evolution correctly. In addition, the presence or absence of cloudiness must be carefully determined to retrieve many atmospheric and surface parameters correctly, because of the fact that, for many of these retrievals, cloud cover (even thin cirrus) is representative of contamination.

This paper reports a procedure that is able to distinguish overcast sky from clear sky with four confidence levels for five different cloud types. The process is applied to 64 daytime images (one per day ranging from 20 January to 20 February and from 20 July to 20 August 2002). These images were acquired in the Mediterranean Sea basin area of Apulia, in the south of Italy. The input data are the reflectances and the radiances contained in the products MOD021KM, relative to the *Terra* mission of the Moderate-Resolution Imaging Spectroradiometer (MODIS; Justice et al. 1998; King et al. 1992). The procedure essentially consists of two stages. In the first stage, beginning from a set of training images and with the aid of the MODIS cloud-mask algorithm (MCMA; Ackerman et al. 1998, 2002), some regions of interest are chosen, one for each test required to identify the differing cloud types. In succession, these regions of interest are suitably averaged to derive spectral signatures, known as end members, and are used in the second stage to analyze the whole image set. Using these end members and the spectral-angle

Corresponding author address: Gennaro Cappelluti, Dipartimento Interateneo di Fisica, Università degli Studi di Bari, Via Amendola 173, 70126 Bari, Italy.
E-mail address: cappelluti@fisica.uniba.it

mapper (SAM) algorithm of classification (Kruse et al. 1993), each time, the process dynamically determines a set of threshold values that are introduced inside the standard algorithm. The MCMA manages these threshold values and the different tests and finally generates the cloud mask.

The advantage of this technique is that the threshold values on which the tests are based do not need to be predetermined from the environmental conditions, because they are obtained by the process of classification, which gathers the pixels having the nearest spectral signatures to the end members in the image.

The criterion used for the selection of the utilized electromagnetic bands is derived from previous works developed with MODIS images and makes the technique also applicable to Meteosat Second-Generation (MSG; Woick et al. 1997; Schmetz et al. 1998; Watts et al. 1998) images. This aspect is important because of the fact that MSG satellites generate images every 15 min, making them the best solution in forecasting with regard to time. The analysis by Meteosat data can be integrated with MODIS data. This last sensor has a limited temporal cover (one, or at the most, two images of the same geographical area per day) but has several bands that are very useful in discriminating the different cloud types. For example, the band centered on the wavelength of 1.38 μm, absent in the MSG data, is particularly useful for the study of thin and high clouds such as cirrus (Gao et al. 2002).

2. MODIS cloud-mask algorithm

Clouds are generally characterized by reflectances and temperatures that are respectively higher and lower than those on the underlying earth's surface. Simple visible and infrared window threshold approaches are often used in cloud detection, albeit with the difficulties they present. Many conditions of the terrestrial surface reduce cloud contrast in some spectral regions (e.g., bright clouds over snow and ice). Moreover, cloud types such as thin cirrus, low-level stratus at night, and small cumulus typically have low contrast with the underlying background. Cloud edges cause further difficulty because the instrument field of view is almost always neither completely obstructed by clouds nor completely clear (Ackerman et al. 2002).

To determine the confidence level of observing clear sky, the MCMA uses several cloud-detection tests. It identifies several domains according to the surface type and the solar illumination, including land, water, snow, ice, desert, and coast, in both daytime and nighttime. Once a pixel has been assigned to a particular domain (defining an algorithm path), a series of threshold tests attempt to detect the presence of clouds in the instrument field of view. Each cloud-detection test returns a confidence level that a given pixel is clear, ranging in value from 1 (high confidence that the pixel is clear) to 0 (high confidence that the pixel is cloudy). Tests capable of detecting similar cloud conditions are grouped together. The MCMA gathers its cloud confidence tests into five sets. These groups are arranged so that independence among them is maximized (Ackerman et al. 2002).

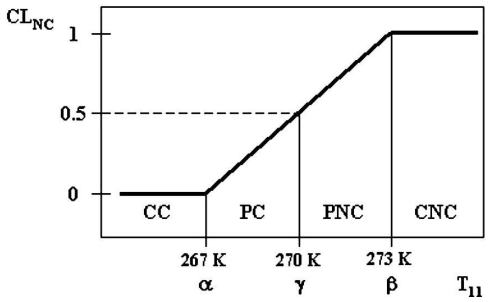

FIG. 1. Plot of CL_{NC} as a function of T_{11} values.

All of the spectral cloud-detection tests rely on thresholds, which are never global and need to be interpreted carefully. For example, if over open ocean (away from sunglint) the brightness temperature at the wavelength of 11 μm (T_{11}) is greater than 270 K, then the pixel is identified as clear. It seems, however, unrealistic to label a pixel with $T_{11} = 271$ K as clear and a neighboring pixel with $T_{11} = 269$ K as cloudy. Figure 1 is a graphical representation of how a confidence level is assigned by the MCMA for a given spectral test. The abscissa represents the observation (T_{11} in the example) and the ordinate is the clear-sky confidence level (CL_{NC}). This test labels an observation greater than the value β as a high-confidence clear-sky scene and assigns it the value of 1. A pixel having a value of less than α is considered to be a cloudy sky observation, and a confidence level of 0 is thus assigned. For observations between α and β, a confidence value between 0 and 1 is assigned according to a linear function. High-confidence cloudy and clear-sky thresholds, α and β, respectively, are derived from previous studies, observations, and theoretical simulations.

The satellite-measured solar reflectances and brightness temperatures (the blackbody temperatures determined using Planck's function) are denoted as ρ and T, respectively. Subscripts refer to the wavelength at which the measurement is made.

Group I detects high, thick clouds using the brightness temperatures T_{11}, $T_{13.9}$, and $T_{6.7}$. Group II is focused on the detection of thin clouds with the brightness temperature differences of $T_{11} - T_{12}$, $T_{8.6} - T_{11}$,

$T_{3.7} - T_{11}$, and $T_{6.7} - T_{11}$. Group III is useful for the detection of low clouds and uses the reflectances $\rho_{0.87}$, $\rho_{0.66}$, and $\rho_{0.94}$, reflectance ratio tests, and the brightness temperature difference $T_{3.7} - T_{3.9}$. Group IV contributes to a good detection of upper-tropospheric thin clouds by the reflectance $\rho_{1.38}$. Group V focuses on the detection of cirrus using the brightness temperature differences $T_{11} - T_{12}$, $T_{3.7} - T_{12}$, and $T_{13.7} - T_{13.9}$.

Tests within a group may detect more than one cloud type, and it is important to realize that the cloud-mask tests are not independent of one another either within the various groups or within the same group. A variety of spectral observations increase the possibility of determining cloud presence. Spectral tests carried out for a spectral region can solve problems that may be encountered with spectral tests performed for another spectral region.

Once the entire test set has been performed, it becomes necessary to combine the results to obtain the overall confidence level Q. The result of the generic test t, belonging to the group $g(t)$, is denoted as $F_t^{g(t)}$. The confidence indicator G_g of group g is the smallest of all the confidence indicators F_t^g belonging to group g and provides information regarding the absence of the cloud type detected by group g. The cloud mask Q is then determined by the geometric average of all the group confidences G_g.

This approach is conservative in the estimation of clear sky. If a test is highly confident that the scene is cloudy ($F_t^g = 0$), the value of Q will be 0.

Cloud masks report four levels of confidence, provided that the field of view is not obstructed by clouds: pixels with $0 \leq Q \leq 0.66$, $0.66 < Q \leq 0.95$, $0.95 < Q \leq 0.99$, and $0.99 < Q \leq 1$ are labeled respectively as confident cloudy (CC), probably cloudy (PC), probably clear (PNC), and confidently clear (CNC). The abovementioned Q threshold values are derived from a statistical analysis based on a considerable number of observations (Ackerman et al. 2002).

3. Dynamic-threshold cloud-mask algorithm

Thresholds used in the MCMA can be found in Ackerman et al. (2002) and are dependent upon a considerable number of parameters, such as

- the hour (because of solar contribution, the different observed objects have reflectance and brightness temperature values that are higher if measured in the daytime and lower if measured at night, making daytime thresholds greater than the nighttime thresholds),
- the month (because of solar contribution, a summer threshold is, e.g., greater than a winter threshold),
- the latitude (e.g., at the equator there are threshold values that are greater than those at the North Pole),
- the ecosystem (an area rich in vegetation and a desert are characterized, e.g., by unequal thresholds),
- the underlying surface (the threshold values vary according to whether there is the ocean or a tilled land under the cloud system, because of the different emissivities of these surfaces),
- the atmospheric conditions (a snowstorm threshold differs from a clear-sky threshold),
- the atmospheric composition (humid days and dry days yield differing threshold values because of the different physical behavior of the individual components of the atmosphere), and
- the aerosol content (it is taken for granted that, over open ocean or in the immediate vicinity of the Etna volcano while in eruption, differing threshold values would be present).

The threshold values used in the MCMA refer to oceans, deserts, or inland areas, which are zones characterized by stable conditions. Apulia is a region in which land and sea are in close proximity and in which there is a wide variety of ecosystems; therefore, it constitutes a very complex environmental system, and the strict thresholds employed by the MCMA are unsuitable. For this reason, an alternative method has had to be employed and the dynamic-threshold cloud-mask algorithm (DTCMA) has been developed accordingly.

DTCMA uses six MODIS bands (one having the sun as blackbody and five having the earth as blackbody): the solar band is 26 (1.375 μm), and the earth infrared bands are 20 (3.750 μm), 21 (3.959 μm), 29 (8.550 μm), 31 (11.030 μm), and 32 (12.020 μm).

The MODIS files used are the products MOD021KM and MOD03 (MODIS *Terra* data products, obtained online at http://daac.gsfc.nasa.gov/data/dataset/MODIS/), all of which are hierarchical data format (HDF) files [National Center for Supercomputing Applications (NCSA) HDF, described online at http://hdf.ncsa.uiuc.edu/]. The MOD021KM products provide data that refer to all of the MODIS bands with a spatial resolution equal to 1 km. They are of L1B type (described online at http://daac.gsfc.nasa.gov/data/dataset/MODIS/) and contain, among other information, the reflectances and the radiances of the objects observed by the sensor. Products MOD03 are of L1A type (described online at http://daac.gsfc.nasa.gov/data/dataset/MODIS/) and contain, in addition, the land–sea maps of the observed scenes.

The reflectance ρ of a pixel is calculated by dividing the reflectance ρ_0 stored in the MOD021KM product by the cosine of the solar zenith angle ϕ_S; the brightness

TABLE 1. Cloud-detection tests used in the work. The header variables are defined in the text.

t	g	τ_g	Z_t	Ω_t
1	1	High, thick clouds	T_{11}	0.05
2	2, 5	Thin clouds, cirrus	$T_{11} - T_{12}$	0.05
3	2	Thin clouds	$T_{8.6} - T_{11}$	0.08
4	2	Thin clouds	$T_{3.7} - T_{11}$	0.12
5	3	Low clouds	$T_{3.7} - T_{3.9}$	0.11
6	4	Upper-tropospheric thin clouds	$\rho_{1.38}$	0.08
7	5	Cirrus	$T_{3.7} - T_{12}$	0.11

temperature is derived from the radiances $B_\lambda(T)$ by applying Planck's law.

The reflectances ρ and the brightness temperatures T are not correct for atmospheric effects, because of the fact that the analyzed bands are positioned inside atmospheric windows, where such effects can be overlooked (Justice et al. 1998; King et al. 1992).

Classification algorithms such as "minimum distance," "parallelepiped," and "k means" are based on spectral intensities, whereas the "maximum likelihood" requires the knowledge of "a priori" probabilities, which are not always known. In contrast, the SAM algorithm is independent of spectral values and does not need the introduction of additional a priori probabilities (Kruse et al. 1993; Ball and Hall 1967; Green et al. 1988). For each class C_r to be determined, the SAM algorithm averages the vectors representing in the space of characteristics the training pixels pertinent to the region of interest $\mathbf{R}_r$ and thus generates the average vector $\mathbf{M}_r$, known as the end member. Once all of the end members have been generated, for each pixel P of the image, SAM calculates the angles ψ_r between the

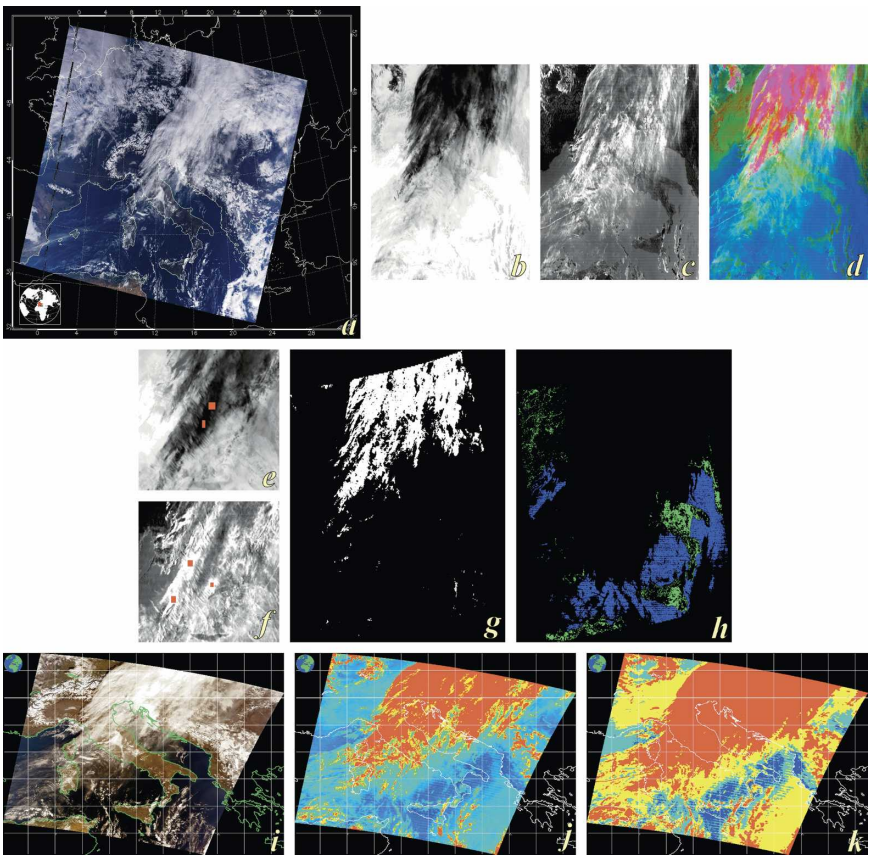

FIG. 2. (a) Visible-spectrum image of the scene observed by MODIS *Terra* at 1010 UTC 26 Jan 2002; grayscale images of (b) $\mathbf{Z}_1$ and (c) $\mathbf{Z}_2$; (d) RGB of the first three bands of the MNF transformation; some of the regions of interest selected for (e) $\mathbf{Z}_1$ and (f) $\mathbf{Z}_2$; (g) thematic map of C_1; (h) thematic map of C_8 and C_9; (i) visible-spectrum image of the MODIS subscene analyzed by DTCMA; (j) image of the matrix $\mathbf{Q}$ (red, yellow, green, cyan, and blue correspond to confidence levels equal to 0, 0.25, 0.5, 0.75, and 1, respectively); (k) cloud mask (the levels of confidence CC, PC, PNC, and CNC are represented with the colors red, yellow, cyan, and blue, respectively) referring to 26 Jan 2002.

TABLE 2. Winter end-member components (all expressed in kelvins, except the sixth one, which is nondimensional).

t	1	2	3	4	5	6	7
$\mathbf{E}_1^t$	234.682	0.660 11	1.485 89	36.2730	18.0143	0.259 671	36.9332
$\mathbf{E}_2^t$	259.379	3.609 01	2.417 62	33.2496	11.5313	0.080 495	36.8776
$\mathbf{E}_3^t$	248.056	2.370 63	3.466 03	34.4896	12.4254	0.145 287	36.8709
$\mathbf{E}_4^t$	240.673	1.151 90	1.190 64	45.2143	18.2874	0.214 754	46.3703
$\mathbf{E}_5^t$	241.182	0.425 91	0.069 15	44.7467	20.8222	0.247 904	45.1763
$\mathbf{E}_6^t$	234.627	0.575 91	1.369 46	34.5712	17.6514	0.296 442	35.1446
$\mathbf{E}_7^t$	241.135	1.311 49	1.272 31	45.7476	18.2087	0.210 822	47.0599
$\mathbf{E}_8^t$	287.967	0.254 40	−2.867 63	7.7989	4.0604	0.001 605	8.0519
$\mathbf{E}_9^t$	284.443	0.635 45	−2.718 05	2.9581	1.9457	0.001 263	3.5954

vector $\mathbf{P}$ associated with the pixel and the various end members $\mathbf{M}_r$. In succession, for each class C_r, the algorithm compares angle ψ_r with the spectral angle Ω_r of class C_r, and if ψ_r is less than Ω_r then the pixel P is considered to belong to class C_r. If two or more classes satisfy that condition, the algorithm of classification labels pixel P with the name of the class minimizing ψ_r. If no class satisfies that condition, pixel P is labeled as "unclassified." The spectral angle Ω_r is the n-dimensional solid angle that defines the opening angle of the n-dimensional cone having the direction of the end member $\mathbf{M}_r$ as axis and that contains all of the pixels belonging to class C_r.

Table 1 for each test t performed demonstrates the group g to which the test belongs, the cloud type τ_g detected by the group, the input quantity Z_t analyzed by the test, and the spectral angle Ω_t used to select from the scene the pixels that can be considered as being contaminated by the cloud type τ_g. In our case, the space of characteristics in which the various pixels are represented has seven dimensions.

Starting from the data contained in the products MOD021KM, for each image a program written in Interactive Data Language produces a file containing a three-dimensional matrix $\mathbf{Z}$ with seven layers ($\mathbf{Z}_1$, $\mathbf{Z}_2$, . . . , $\mathbf{Z}_7$). The generic dataset $\mathbf{Z}_t$ is the bidimensional matrix that contains the values of the quantity computed by test t. The dimensions of every matrix $\mathbf{Z}_t$ are the shortest ones that allow $\mathbf{Z}_t$ to contain all of the pixels from the Italian geographical area stored in the original MODIS image, the only pixels processed by the algorithm. The construction of the file with the seven layers $\mathbf{Z}_1$, $\mathbf{Z}_2$, . . . , $\mathbf{Z}_7$ is necessary to apply the algorithm of classification in a seven-dimensional space of characteristics.

Once this file has been produced, the following eight steps are performed:

1) Using the proprietary "ENVI" software package, for each layer $\mathbf{Z}_t$ a region of interest $\mathbf{R}_t$ (ENVI User's Guide Team 2003), constituted by pixels typical of cloud type $\tau_{g(t)}$ being detected (Figs. 2e and 2f), is manually selected in $\mathbf{Z}_t$ following the MCMA test logic.
2) The SAM algorithm of classification, making use of the newly determined regions of interest $\mathbf{R}_1$, $\mathbf{R}_2$, . . . , $\mathbf{R}_7$, generates the end members $\mathbf{M}_1$, $\mathbf{M}_2$, . . . , $\mathbf{M}_7$ in the seven-dimensional space of characteristics and, by using these end members and the spectral angles Ω_1, Ω_2, . . . , Ω_7 shown in Table 1 (expressed in radians), produces seven thematic maps, containing classes C_1, C_2, . . . , C_7, respectively, where the generic class C_t is constituted by the pixels located within the seven-dimensional cone determined by the end member $\mathbf{M}_t$ and the spectral angle Ω_t (Fig. 2g).
3) For every layer t, the following two averages are calculated: the average mcl_t of the pixels belonging to matrix $\mathbf{Z}_t$ and contained inside the intersection between set C_t and land pixel set Σ_L and the average mcs_t of tth-layer pixels belonging to the intersection between set C_t and sea pixel set Σ_S (Σ_L and Σ_S sets are obtained from the land–sea maps provided by the MODIS MOD03 products).
4) Set Σ_C (the union set of sets C_t) and set Σ_{NC} (the complementary set of set Σ_C) are built.
5) Inside the intersection between set Σ_{NC} and sets Σ_L and Σ_S, respectively, a region of interest $\mathbf{R}_8$ repre-

TABLE 3. Winter end-member-component standard deviations (all expressed in kelvins, except the sixth one, which is nondimensional).

t	1	2	3	4	5	6	7
σ_1^t	11.828	0.514 97	0.986 40	8.6932	4.3884	0.133 598	8.4489
σ_2^t	8.719	0.838 71	1.417 86	7.1138	2.6251	0.045 680	7.6451
σ_3^t	9.228	0.989 75	1.107 97	7.0302	3.5131	0.070 640	7.0614
σ_4^t	13.734	0.645 97	1.247 92	9.6138	3.9222	0.136 894	9.3827
σ_5^t	18.672	0.222 11	1.867 10	9.7413	4.5584	0.181 308	9.7635
σ_6^t	13.680	0.511 00	0.801 57	9.2765	5.6999	0.138 071	8.9021
σ_7^t	13.887	0.823 76	1.149 17	10.1977	4.3029	0.136 484	9.9396
σ_8^t	3.640	0.181 97	0.350 49	1.2016	0.7702	0.000 855	1.2146
σ_9^t	1.953	0.230 51	0.386 52	0.3255	0.2915	0.000 443	0.4797

TABLE 4. Summer end-member components (all expressed in kelvins, except the sixth one, which is nondimensional).

t	1	2	3	4	5	6	7
$\mathbf{E}_1^t$	231.841	0.255 96	0.923 64	32.6617	17.6898	0.378 934	32.9243
$\mathbf{E}_2^t$	279.019	4.547 99	0.462 71	33.2258	9.6683	0.028 595	37.8477
$\mathbf{E}_3^t$	250.988	2.128 26	2.732 82	33.1294	10.9150	0.118 336	35.2858
$\mathbf{E}_4^t$	257.182	0.592 71	−0.906 80	49.4095	17.6935	0.102 363	49.9973
$\mathbf{E}_5^t$	256.725	0.415 57	−1.009 63	47.7078	18.9190	0.132 662	48.1237
$\mathbf{E}_6^t$	231.048	0.304 50	1.033 06	34.6811	19.0124	0.402 523	34.9894
$\mathbf{E}_7^t$	258.867	0.904 81	−0.740 15	49.7123	17.2947	0.087 902	50.6246
$\mathbf{E}_8^t$	308.398	2.050 98	−3.969 87	12.1050	2.9851	0.000 302	14.1661
$\mathbf{E}_9^t$	293.323	1.092 13	−3.047 99	6.7620	2.2321	0.000 798	7.8543

sentative of clear sky over land and a region of interest $\mathbf{R}_9$ for clear sky over sea are selected.

6) Starting from the regions of interest $\mathbf{R}_8$ and $\mathbf{R}_9$, the classification algorithm generates the end members $\mathbf{M}_8$ and $\mathbf{M}_9$, and, by using these end members and spectral angles Ω_8 and Ω_9 (equal to 0.006 and 0.003 radians, respectively), a thematic map with two families of pixels (the land clear-sky pixel class C_8 and the sea clear-sky pixel class C_9) is produced (Fig. 2h).
7) The average mncl_t of the tth-layer pixels contained inside C_8 and the average mncs_t of the matrix $\mathbf{Z}_t$ pixels belonging to C_9 are calculated for every t.
8) For each layer t, a pair of values (mcl_t, mncl_t) is assigned to all of the land pixels and a pair (mcs_t, mncs_t) is assigned to all of the sea values.

The images in Fig. 2 were obtained using the MODIS data of 1010 UTC 26 January 2002. Starting from the top-left-hand side, there are the red–green–blue (RGB) image of MODIS bands 1, 4, and 3 (respectively centered on 0.635, 0.555, and 0.469 μm), which is registered according to the universal transverse Mercator (UTM) projection technique with the 1984 world geodetic system datum (WGS84) and north zone 33 (Fig. 2a); the grayscale images of layers $\mathbf{Z}_1$ and $\mathbf{Z}_2$ (Figs. 2b,c), which respectively give prominence to high, thick clouds ($\mathbf{Z}_1$) and thin clouds and cirrus ($\mathbf{Z}_2$); and the RGB image of the first three bands of minimum noise fraction (MNF) transformation (Fig. 2d) (Nielsen 1999). Figure 2 also contains some regions of interest selected for the $\mathbf{Z}_1$ and $\mathbf{Z}_2$ matrices (Figs. 2e,f), the thematic map of the cloud type analyzed by the first test (Fig. 2g), and the land and sea clear-sky thematic map (Fig. 2h). Figures 2i, 2j, and 2k respectively report the visible band image of the MODIS subscene, which is analyzed by DTCMA, the image of the matrix $\mathbf{Q}$, and the final cloud mask image.

For every layer $\mathbf{Z}_t$ the corresponding region of interest $\mathbf{R}_t$ is highlighted following the indications of test t. For example, region $\mathbf{R}_2$ is obtained by selecting from image $\mathbf{Z}_2$ the whitest pixels, which correspond to the greatest values of $T_{11} - T_{12}$ and so to cloudy pixels (thin clouds), according to test-2 logic.

Because the objective is to study Apulia, the regions of interest (see points 1 and 5 of the list above) were selected with preference to those in close proximity to Apulia and the whole of Italy and not, for example, those in Africa or northern Europe. This procedure was used because many characteristics of cloud systems strongly depend upon the zone in which they are situated, and thus using samples drawn from other zones would have increased the risk of considerable classification errors. Because of this approach, the obtained results are optimized for Apulia.

For clear-sky areas, it is necessary to verify accurately that the selected regions of interest are truly representative of clear sky and are lacking in contamination by cloudy elements. The clear-sky regions of interest were selected to be at a sufficient distance from cloudy pixels in every layer $\mathbf{Z}_t$.

The spectral angles $\Omega_1, \Omega_2, \ldots, \Omega_9$ used in the various SAM classifications to derive classes $C_1, C_2, \ldots, C_9$ (Table 1 and point 6 above) were obtained by selecting, for each training image, a new set $\mathbf{R}'_{11}, \mathbf{R}'_2, \ldots, \mathbf{R}'_9$ of regions of interest with the same method employed for $\mathbf{R}_1, \mathbf{R}_2, \ldots, \mathbf{R}_9$ (points 1 and 5 above), tuning the spectral angles to make $C_1, C_2, \ldots, C_9$ contain approximately all of the pixels of $\mathbf{R}'_1, \mathbf{R}'_2, \ldots, \mathbf{R}'_9$, respectively,

TABLE 5. Summer end-member-component standard deviations (all expressed in kelvins, except the sixth one, which is nondimensional).

t	1	2	3	4	5	6	7
σ_1^t	13.490	0.268 49	0.439 86	9.1008	6.1490	0.180 356	8.9186
σ_2^t	7.623	1.009 81	1.394 99	6.3743	1.9756	0.018 377	7.2548
σ_3^t	8.620	0.787 15	1.456 73	7.8516	2.6898	0.031 541	8.4585
σ_4^t	11.644	0.338 34	0.754 41	13.0282	3.6260	0.060 645	13.1538
σ_5^t	19.087	0.242 33	1.195 68	12.6636	4.5488	0.128 848	12.8201
σ_6^t	13.042	0.421 14	0.468 89	7.1080	6.2660	0.172 464	6.8961
σ_7^t	12.161	0.325 88	0.736 22	11.0013	3.1060	0.052 578	11.1806
σ_8^t	8.003	0.610 22	0.373 85	1.5435	0.6974	0.000 808	2.0600
σ_9^t	2.097	0.390 73	0.426 40	2.9266	1.4417	0.000 381	2.7441

TABLE 6. Standard deviation (°) of the angle between winter end members and averages.

σ_1	σ_2	σ_3	σ_4	σ_5	σ_6	σ_7	σ_8	σ_9
3.28	2.28	2.54	3.42	3.85	3.60	3.62	0.36	0.15

TABLE 7. Standard deviation (°) of the angle between summer end members and averages.

σ_1	σ_2	σ_3	σ_4	σ_5	σ_6	σ_7	σ_8	σ_9
3.74	2.14	2.72	4.17	4.39	3.17	3.60	0.56	0.78

and averaging all of the training image spectral angles that facilitated the arrival at such a condition.

The spectral angles indicated in Table 1 and point 6 above were derived from MCMA in an empirical way. In fact, following the indication given by MCMA thresholds, regions of interest typical of the different sky types were selected. In succession, the spectral angles were determined so as to maximize the SAM skill in detecting the different sky types by using the chosen regions of interest. Even if derived in an empirical manner, the spectral angles are related to the sky-type characteristics. The spectral angles depend on the position and the variability of the different sky-type classes in the space of characteristics: the lesser the width of the angle between the end members of two different classes is and the smaller the two classes are, the less wide the spectral angles necessary to discern the two classes are.

The quantities $\mathrm{mc}_t(x, y)$ and $\mathrm{mnc}_t(x, y)$ can be considered as coinciding with the quantities α and β of section 2, and the levels of confidence produced by the new approach are given by equations such as

$$F_t^{g(t)}(x, y) = \begin{cases} 0 & \text{if} \quad Z_t(x, y) < \mathrm{mc}_t(x, y) \\ \dfrac{Z_t(x, y) - \mathrm{mc}_t(x, y)}{\mathrm{mnc}_t(x, y) - \mathrm{mc}_t(x, y)} & \text{if} \quad \mathrm{mc}_t(x, y) \le Z_t(x, y) \le \mathrm{mnc}_t(x, y) \\ 1 & \text{if} \quad Z_t(x, y) > \mathrm{mnc}_t(x, y). \end{cases} \tag{1}$$

This kind of equation is applied to each pixel (x, y) of each layer $\mathbf{Z}_t$, producing a new file containing the three-dimensional matrix $\mathbf{F}$, made by the seven layers $\mathbf{F}_1^1$, $\mathbf{F}_2^{2,5}$, $\mathbf{F}_3^2$, $\mathbf{F}_4^2$, $\mathbf{F}_5^3$, $\mathbf{F}_6^4$, and $\mathbf{F}_7^5$.

According to the MCMA scheme (Ackerman et al. 2002), for each pixel (x, y) from the values of $F_t^g(x, y)$ the value of $G_g(x, y)$ is drawn. Therefore, the algorithm builds a further file containing the three-dimensional matrix $\mathbf{G}$ with the five layers $\mathbf{G}_1$, $\mathbf{G}_2$, $\mathbf{G}_3$, $\mathbf{G}_4$, and $\mathbf{G}_5$, where

$$G_1(x, y) = F_1^1(x, y), \tag{2}$$

$$G_2(x, y) = \min[F_2^{2,5}(x, y), F_3^2(x, y), F_4^2(x, y)], \tag{3}$$

$$G_3(x, y) = F_5^3(x, y), \tag{4}$$

$$G_4(x, y) = F_6^4(x, y), \quad \text{and} \tag{5}$$

$$G_5(x, y) = \min[F_2^{2,5}(x, y), F_7^5(x, y)]. \tag{6}$$

Thus, according to the MCMA, the value of $Q(x, y)$ is obtained from the values of $G_g(x, y)$ for each pixel (x, y) with the relationship

$$Q(x, y) = \left[\prod_{g=1}^{5} G_g(x, y)\right]^{1/5}. \tag{7}$$

Last, pixels with $0 \le Q(x, y) \le 0.66$ are labeled as CC, pixels with $0.66 < Q(x, y) \le 0.95$ are labeled as PC, pixels with $0.95 < Q(x, y) \le 0.99$ are labeled as PNC, and pixels with $0.99 < Q(x, y) \le 1$ are labeled as CNC (Figs. 2i,j,k).

The procedure described was applied to 10 winter MODIS images and 10 summer MODIS images (training sets). For each image ($d = 1, 2, \ldots, 10$) of each training set ($p = w, s$), where w indicates winter and s indicates summer, the average value $\mathbf{M}_r^t(p, d)$ of the values referring to the pixels belonging to the region of interest $\mathbf{R}_r(p, d)$ is calculated for every matrix $\mathbf{Z}_t(p, d)$, with $r = 1, 2, \ldots, 9$ and $t = 1, 2, \ldots, 7$. For each season, the tth component $\mathbf{E}_r^t(p)$ of the end member $\mathbf{E}_r(p)$ associated with the region of interest $\mathbf{R}_r$ is the arithmetic average of the values $\mathbf{M}_r^t(p, d)$ along the 10 training images of season p:

$$\mathbf{E}_r^t(w) = \frac{1}{10}\sum_{d=1}^{10} \mathbf{M}_r^t(w, d) \quad \text{and} \tag{8}$$

$$\mathbf{E}_r^t(s) = \frac{1}{10}\sum_{d=1}^{10} \mathbf{M}_r^t(s, d). \tag{9}$$

TABLE 8. Student's t test probability of winter and summer end members being separated.

P_1	P_2	P_3	P_4	P_5	P_6	P_7	P_8	P_9
0.71	0.75	0.68	0.65	0.65	0.63	0.65	1.00	1.00

TABLE 9. Annual end-member components (all expressed in kelvins, except the sixth one, which is nondimensional).

t	1	2	3	4	5	6	7
$\mathbf{E}_1^t$	233.261	0.458 04	1.204 76	34.4674	17.8521	0.319 303	34.9287
$\mathbf{E}_2^t$	269.199	4.078 50	1.440 16	33.2377	10.5998	0.054 545	37.3626
$\mathbf{E}_3^t$	249.522	2.249 44	3.099 43	33.8095	11.6702	0.131 812	36.0784
$\mathbf{E}_4^t$	248.928	0.872 30	0.141 92	47.3119	17.9904	0.158 559	48.1838
$\mathbf{E}_5^t$	248.954	0.420 74	−0.470 24	46.2272	19.8706	0.190 283	46.6500
$\mathbf{E}_6^t$	232.837	0.440 21	1.201 26	34.6261	18.3319	0.349 483	35.0670
$\mathbf{E}_7^t$	250.001	1.108 15	0.266 08	47.7299	17.7517	0.149 362	48.8422

The end members so determined (Tables 2, 3, 4, and 5) were used rather than choosing regions of interest (points 1 and 5 of section 3) so as to analyze the whole image dataset.

4. Results

For each training image, the choice of the various regions of interest $\mathbf{R}_r(p, d)$ involves the determination of the nine average vectors $\mathbf{M}_r(p, d)$, with the seven components $\mathbf{M}_r^1(p, d), \mathbf{M}_r^2(p, d), \ldots, \mathbf{M}_r^7(p, d)$. The end members $\mathbf{E}_r(p)$ are the averages of the vectors $\mathbf{M}_r(p, d)$ related to the 10 training images of season p. Tables 6 and 7 list the values assumed by the standard deviation $\sigma_r(p)$ of the angle between vectors $\mathbf{E}_r(p)$ and $\mathbf{M}_r(p, d)$, calculated using the following formula:

$$\sigma_r(p) = \left[\frac{1}{10} \sum_{d=1}^{10} \arccos^2 \frac{\mathbf{E}_r(p) \cdot \mathbf{M}_r(p, d)}{|\mathbf{E}_r(p)||\mathbf{M}_r(p, d)|} \right]^{1/2}. \tag{10}$$

The average angular distance between the winter end members is equal to 6.22°; the maximum value occurs with $\mathbf{E}_7$ and $\mathbf{E}_9$ ($\theta_{79} = 14.79°$), and the minimum is between $\mathbf{E}_4$ and $\mathbf{E}_7$ ($\theta_{47} = 0.17°$). The minute value of θ_{47} was foreseeable because thin clouds and cirrus characteristics are so close that there are even quantities (such as $T_{11} - T_{12}$, evaluated by test 2) that detect both cloud types. The same reasoning can also be adopted for other cloud types.

For summer, the average angular distance between the end members is 5.98° and the maximum and the minimum values occur again with $\mathbf{E}_7$ and $\mathbf{E}_9$ ($\theta_{79} = 13.70°$) and with $\mathbf{E}_4$ and $\mathbf{E}_7$ ($\theta_{47} = 0.15°$), respectively. The previous angles θ_{ij} between the end members $\mathbf{E}_i(p)$ and $\mathbf{E}_j(p)$ were calculated with the relationship

$$\theta_{ij}(p) = \arccos \frac{\mathbf{E}_i(p) \cdot \mathbf{E}_j(p)}{|\mathbf{E}_i(p)||\mathbf{E}_i(p)|}. \tag{11}$$

For each couple of end members ($\mathbf{E}_i$, $\mathbf{E}_j$) from the same season p, the Student's t test was performed to estimate whether end members $\mathbf{E}_i$ and $\mathbf{E}_j$ could be considered to be representative of different categories. According to this test, so that the sample constituted by vectors $\mathbf{M}_i(p, 1), \mathbf{M}_i(p, 2), \ldots, \mathbf{M}_i(p, 10)$ and that constituted by vectors $\mathbf{M}_j(p, 1), \mathbf{M}_j(p, 2), \ldots, \mathbf{M}_j(p, 10)$ can be considered with a certain level of confidence to be extracted from different populations, the Student's t test parameter t must be greater than the tabulated critical value t_0. The sample constituted by vectors $\mathbf{M}_i(p, 1), \mathbf{M}_i(p, 2), \ldots, \mathbf{M}_i(p, 10)$ is considered as a reference and has an average $\mu_i = 0°$ and standard deviation $s_i = \sigma_i$, whereas that constituted by vectors $\mathbf{M}_j(p, 1), \mathbf{M}_j(p, 2), \ldots, \mathbf{M}_j(p, 10)$ has an average $\mu_j = \theta_{ij}$ and standard deviation $s_j = \sigma_j$.

For 27 couples ($\mathbf{E}_i$, $\mathbf{E}_j$) over the 36 winter ones we can assert with a confidence level of 90% that the population of vectors $\mathbf{M}_i(w, 1), \mathbf{M}_i(w, 2), \ldots, \mathbf{M}_i(w, 10)$ and that of vectors $\mathbf{M}_j(w, 1), \mathbf{M}_j(w, 2), \ldots, \mathbf{M}_j(w, 10)$ are different and therefore the end members $\mathbf{E}_i$ and $\mathbf{E}_j$ can be considered to be representative of two different categories. For couples ($\mathbf{E}_1$, $\mathbf{E}_3$), ($\mathbf{E}_1$, $\mathbf{E}_5$), ($\mathbf{E}_2$, $\mathbf{E}_6$), and ($\mathbf{E}_3$, $\mathbf{E}_6$) the confidence level is equal to 80%, for couple ($\mathbf{E}_2$, $\mathbf{E}_3$) it is 70%, and for couples ($\mathbf{E}_1$, $\mathbf{E}_6$), ($\mathbf{E}_4$, $\mathbf{E}_5$), ($\mathbf{E}_4$, $\mathbf{E}_7$), and ($\mathbf{E}_5$, $\mathbf{E}_7$) it is equal to 60% (Dowdy and Wearden 1991). Thus, 75% of all the couples of winter end members consist of well-separated end members, and some couples of cloud types (such as high thick clouds and upper-tropospheric thin clouds, thin clouds and low clouds, thin clouds and cirrus, or low clouds and cirrus) have spectral signatures that are too close to

TABLE 10. Annual end-member-component standard deviations (all expressed in kelvins, except the sixth one, which is nondimensional).

t	1	2	3	4	5	6	7
σ_1^t	12.433	0.450 27	0.797 32	8.8578	5.2019	0.166 149	8.7018
σ_2^t	12.847	1.023 84	1.696 98	6.5740	2.4549	0.043 096	7.2708
σ_3^t	8.820	0.879 19	1.314 59	7.2870	3.1422	0.055 010	7.6270
σ_4^t	15.010	0.578 07	1.471 38	11.3496	3.6888	0.118 081	11.2748
σ_5^t	20.032	0.226 30	1.623 19	11.1004	4.5384	0.164 104	11.1934
σ_6^t	13.137	0.476 53	0.662 02	8.0435	5.8715	0.161 495	7.7506
σ_7^t	15.625	0.644 41	1.395 74	10.5226	3.6823	0.118 783	10.4573

TABLE 11. Standard deviation (°) of the angle between annual end members and averages.

σ_1	σ_2	σ_3	σ_4	σ_5	σ_6	σ_7
3.34	2.34	2.57	3.44	3.88	3.60	3.64

allow for their end members to detect only the cloud type they should analyze.

For the summer season, 29 out of 36 couples ($\mathbf{E}_i$, $\mathbf{E}_j$) can be considered, with a confidence level of 90%, to consist of end members representative of two different categories. For couples ($\mathbf{E}_1$, $\mathbf{E}_3$) and ($\mathbf{E}_5$, $\mathbf{E}_6$) the confidence level is equal to 80%, for couple ($\mathbf{E}_2$, $\mathbf{E}_3$) it is 70%, and for couples ($\mathbf{E}_1$, $\mathbf{E}_6$), ($\mathbf{E}_4$, $\mathbf{E}_5$), ($\mathbf{E}_4$, $\mathbf{E}_7$), and ($\mathbf{E}_5$, $\mathbf{E}_7$) it is 60%. Thus, 81% of all the couples of summer end members can be considered to consist of elements that are well separated and that can detect almost exclusively the cloud type that they are required to analyze.

For each sky type ($r = 1, 2, \ldots, 9$) the Student's t test was performed to estimate whether the winter end member $\mathbf{E}_r(w)$ and the summer end member $\mathbf{E}_r(s)$ can be considered to be derived from different populations of averages. The population of vectors $\mathbf{M}_r(w, 1)$, $\mathbf{M}_r(w, 2), \ldots, \mathbf{M}_r(w, 10)$ and the population of vectors $\mathbf{M}_r(s, 1)$, $\mathbf{M}_r(s, 2), \ldots, \mathbf{M}_r(s, 10)$ are different with a confidence level that ranges from 63% to 75% for $r = 1, 2, \ldots, 7$ and that is equal to 99% for $r = 8, 9$ (Table 8). This result means that end members $\mathbf{E}_8$ and $\mathbf{E}_9$ change significantly from winter to summer whereas for the remaining end members ($r = 1, 2, \ldots, 7$) winter and summer populations of averages $\mathbf{M}_r(w, 1)$, $\mathbf{M}_r(w, 2), \ldots, \mathbf{M}_r(w, 10)$ and $\mathbf{M}_r(s, 1)$, $\mathbf{M}_r(s, 2), \ldots, \mathbf{M}_r(s, 10)$ can be considered to belong to the same population and could be used all together to calculate annual end members $\mathbf{E}_r(a)$ (Tables 9, 10, and 11; Fig. 6, below). In moving from winter to summer, it is even possible to observe that components of end members $\mathbf{E}_r$ with $r = 1, 2, \ldots, 7$ vary notably (Table 12) while angles between them only vary slightly (Table 13). The angles θ_r between the end members $\mathbf{E}_r(w)$ and $\mathbf{E}_r(s)$ that are shown in Table 13 were calculated using the formula

$$\theta_r = \arccos \frac{\mathbf{E}_r(w) \cdot \mathbf{E}_r(s)}{|\mathbf{E}_r(w)||\mathbf{E}_r(s)|}. \quad (12)$$

Figures 3, 4, and 5 show some cloud masks produced by this algorithm. For each image there are the RGB of the MODIS bands 1, 4, and 3 (Figs. 3a, 4a, 5a, and 5c) and the cloud mask in UTM, in which the levels of confidence CC, PC, PNC, and CNC are represented with the colors red, yellow, cyan, and blue, respectively (Figs. 3b, 4b, 5b, and 5d).

TABLE 12. Percent differences between summer and winter end-member components.

t	1	2	3	4	5	6	7
ε_1^t	−1.22	−88.24	−46.67	−10.48	−1.82	37.35	−11.48
ε_2^t	7.30	23.02	−135.74	−0.07	−17.58	−95.15	2.60
ε_3^t	1.18	−10.77	−23.66	−4.02	−12.94	−20.45	−4.39
ε_4^t	6.63	−64.10	−1477.90	8.87	−3.30	−70.88	7.53
ε_5^t	6.24	−2.46	−229.41	6.41	−9.58	−60.56	6.32
ε_6^t	−1.54	−61.66	−28.00	0.32	7.42	30.35	−0.44
ε_7^t	7.09	−36.70	−756.34	8.31	−5.15	−82.30	7.30
ε_8^t	6.85	155.86	−32.24	43.27	−30.52	−136.65	55.04
ε_9^t	3.07	52.87	−11.44	78.27	13.71	−45.12	74.39

In Fig. 3, comparing the cloud mask (Fig. 3b) with the visible-band image (Fig. 3a), it is evident that the algorithm correctly classifies as cloudy all of the areas that appear as covered by clouds. The pixels corresponding to the cloud systems over the former Yugoslavia, Apulia, the River Po, Liguria, and in the Corsica region are classified as CC. For the Tyrrhenian Sea area, it is evident that, although in the visible spectrum it seems that there are not many clouds, a considerable number of pixels are labeled as PC and CC. This result derives from the fact that the cloud mask expresses the presence of clouds independently of cloud type. In the considered area, layers such as $\mathbf{Z}_2$ and $\mathbf{Z}_3$ (Figs. 3c,d) have radiance values distant from those characteristic of clear sky, indicating that thin clouds may be present in the examined zone (Fig. 3e).

The PC and CC pixels in the vicinity of the Gargano Promontory (Apulia) that are present in the cloud mask of Fig. 4 are justified by bands such as $\mathbf{Z}_2$ (Figs. 4c–e). The grayscale image of $\mathbf{Z}_6$ in Fig. 4 demonstrates that those clouds are not of the upper-tropospheric thin variety.

When comparing Figs. 5a and 5b, in the area between Calabria and Libya there seems to be an excess of pixels labeled as PC. Layers such as $\mathbf{Z}_4$ (Fig. 5e) have radiances distant from those characteristic of clear sky; thus, the possibility of the presence of thin clouds or particles of sand in that zone must be considered.

Bands such as $\mathbf{Z}_1$ (Fig. 5f) demonstrate that the CC pixels over the Tyrrhenian Sea in the cloud mask of 6 August 2002 are not in excess, as one could surmise by looking at Figs. 5c and 5d.

It is important to add that MCMA performs additional clear-sky restoral tests, which act upon 0.87, 0.66,

TABLE 13. Angles (°) between summer and winter end members.

θ_1	θ_2	θ_3	θ_4	θ_5	θ_6	θ_7	θ_8	θ_9
1.14	0.94	0.72	0.68	0.73	0.44	0.68	1.32	1.09

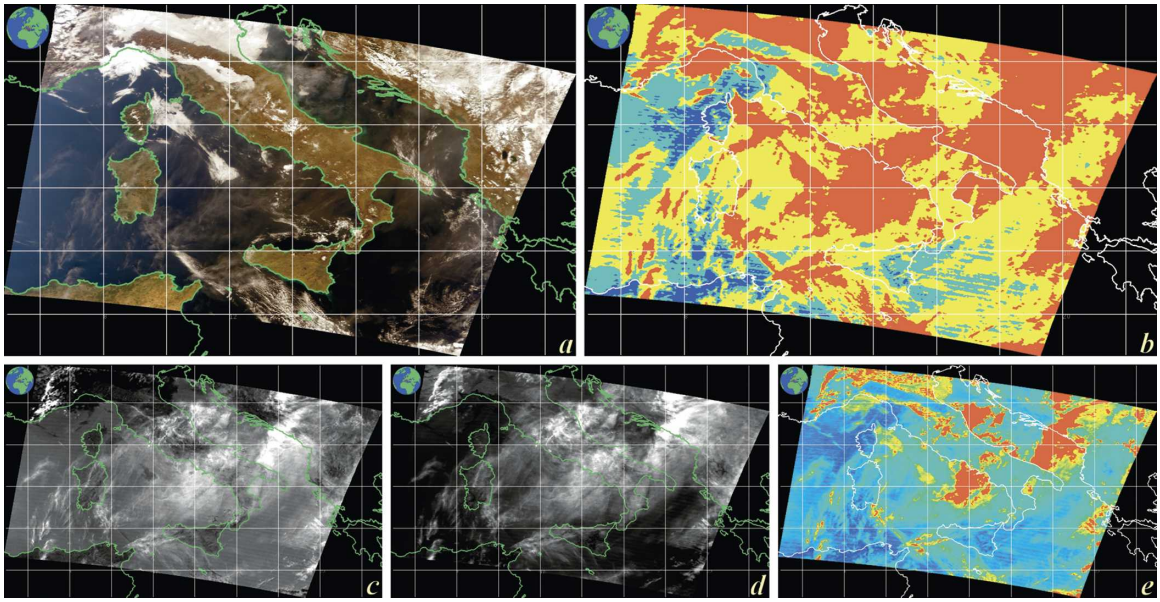

FIG. 3. (a) Visible-band image for 1000 UTC 28 Jan 2002; (b) corresponding cloud mask; (c) grayscale image of $\mathbf{Z}_2$; (d) grayscale image of $\mathbf{Z}_3$; (e) image of the matrix $\mathbf{Q}$.

3.75, 11, 0.895, 0.935, and 0.443 μm. The first two bands are used to restore clear sky for areas characterized by a land–water mix and for regions classified as shallow water, and the remaining ones are used to remove the cloudiness assigned to pixels affected by sunglint. Bands at 3.75 and 11 μm are also employed by DTCMA, but DTCMA does not use any clear-sky restoral test; thus it is possible that sometimes DTCMA

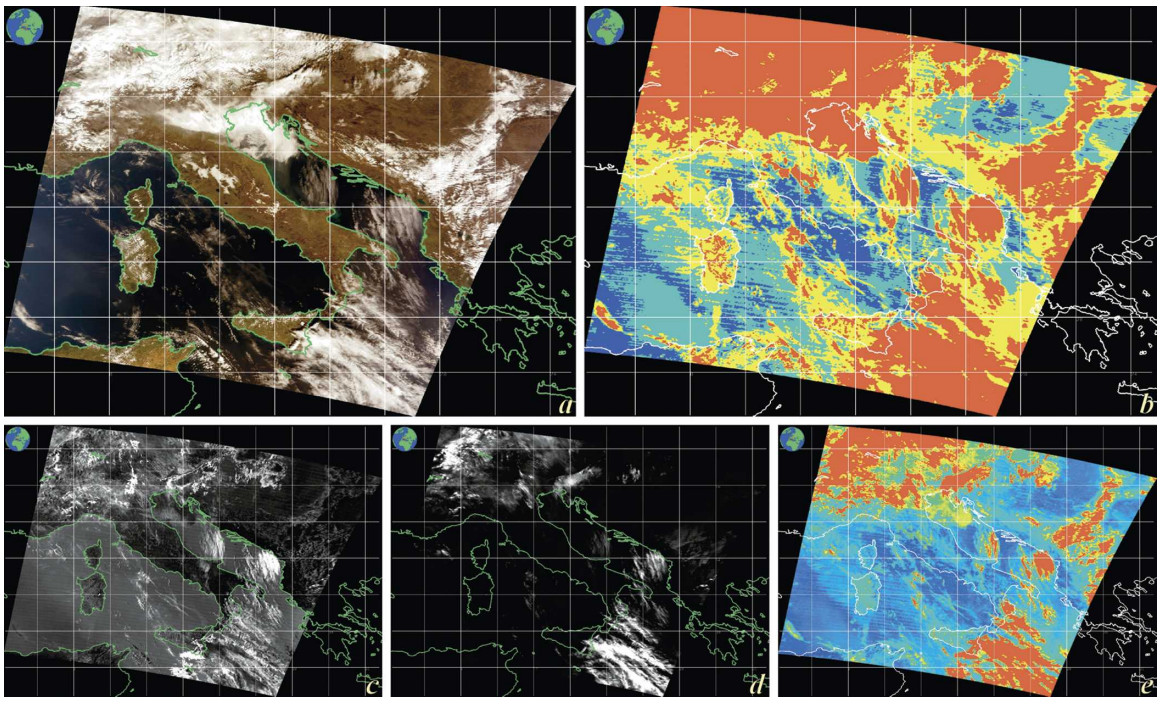

FIG. 4. (a) Visible-spectrum image for 1010 UTC 11 Feb 2002; (b) relative cloud mask; grayscale images of (c) $\mathbf{Z}_2$ and (d) $\mathbf{Z}_6$; (e) image of the matrix $\mathbf{Q}$.

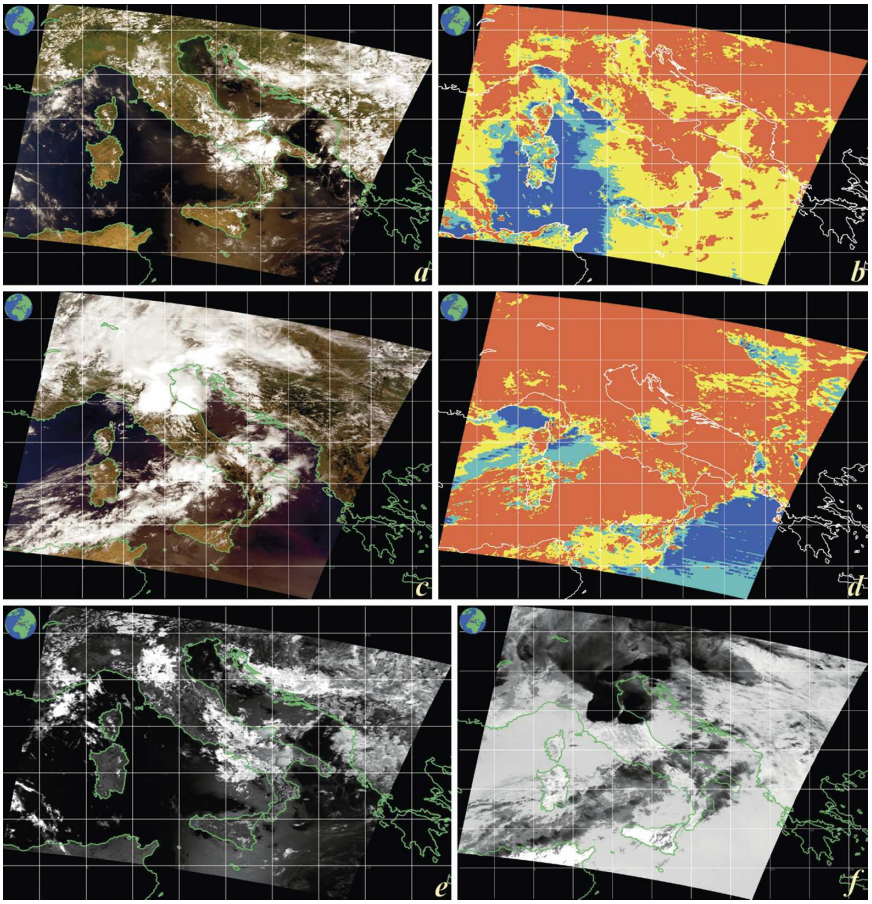

FIG. 5. Visible-band images for (a) 1005 UTC 30 Jul and (c) 1010 UTC 6 Aug 2002; (b), (d) corresponding cloud masks; grayscale images of (e) $\mathbf{Z}_4$ and (f) $\mathbf{Z}_1$.

classifies pixels affected by sunglint as being cloudy (Figs. 3, 4, and 5).

By carefully comparing all of the cloud masks that have been produced by using the annual end members with those obtained by using the winter and summer end members, it is evident that no remarkable differences were observed (Figs. 6, 4b, and 5d).

Figure 7 shows the subimage of the scene observed by MODIS *Terra* in the visible spectrum at 1000 UTC 28 January 2002 (Fig. 7a), the corresponding cloud

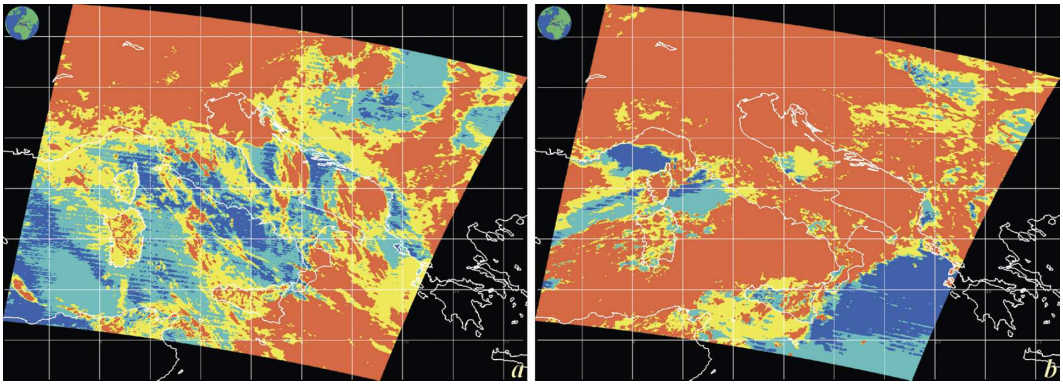

FIG. 6. Cloud masks of the scenes observed on (a) 11 Feb and (b) 6 Aug 2002, both obtained using annual end members.

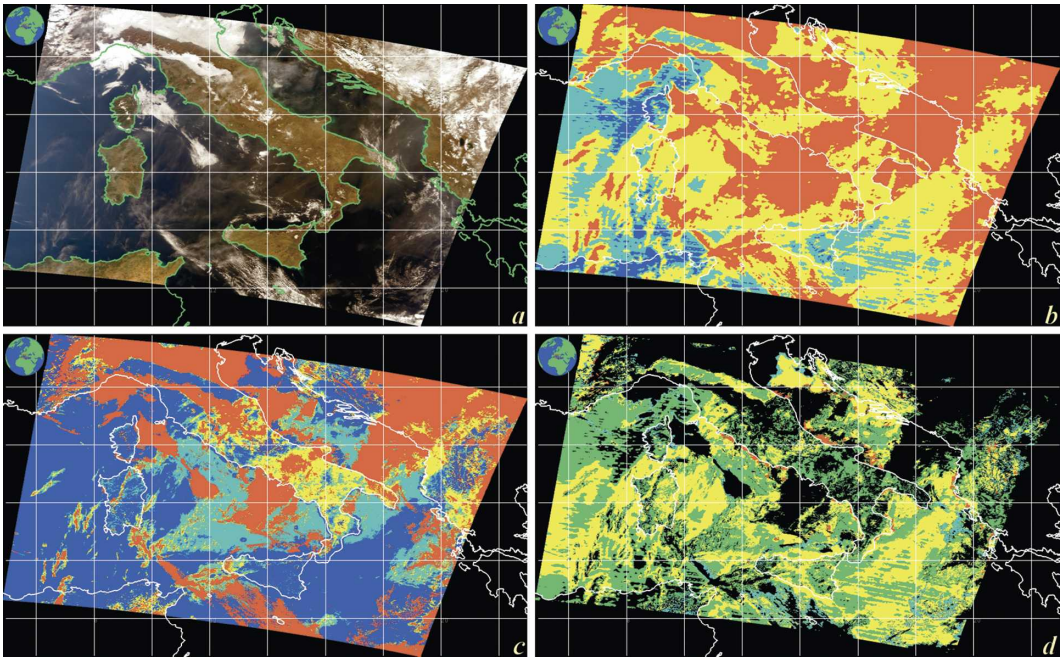

FIG. 7. (a) Visible-band image for 28 Jan 2002; images of (b) DTCM and (c) MCM; (d) DTCM − MCM image (violet, blue, cyan, black, green, yellow, and red correspond to values equal to 3, 2, 1, 0, −1, −2, and −3, respectively).

masks generated by DTCMA (Fig. 7b) and MCMA (Fig. 7c), and the image of the difference of the matrices "DTCM" and "MCM" (Fig. 7d). Pixels classified as CC, PC, PNC, and CNC are stored in DTCM and MCM as integers with values of 0, 1, 2, and 3, respectively, and matrix DTCM − MCM is obtained by subtracting MCM values from DTCM values pixel by pixel. The confusion matrix of the considered subimage (Table 14) provides an overall accuracy that is equal to 35.0%.

By observing Figs. 8, 9, and 10 it is possible to compare DTCMA and MCMA performances for 11 February, 30 July, and 6 August 2002. The overall accuracies given by the confusion matrices of those scenes are equal to 45.1%, 41.8%, and 62.9% respectively (Tables 15, 16, and 17).

Figure 11 reports subimages of DTCM − MCM, DTCM, MCM, visible band scene, $\mathbf{Z}_1$, $\mathbf{Z}_2$, $\mathbf{Z}_3$, and $\mathbf{Z}_6$, all for the same area observed by MODIS *Terra* at 1000 UTC 28 January 2002. Figure 12 shows images of DTCM−MCM, DTCM, MCM, visible spectrum scene, $\mathbf{Z}_2$, and $\mathbf{Z}_4$, referring to an area observed on 30 July 2002.

TABLE 14. Confusion matrix for 28 Jan 2002.

	CC MCM	PC MCM	PNC MCM	CNC MCM
CC DTCM	25.6	6.7	5.8	0.9
PC DTCM	3.8	6.6	10.6	25.1
PNC DTCM	0.0	0.1	0.3	11.8
CNC DTCM	0.0	0.0	0.1	2.6

By carefully comparing all the cloud masks produced using DTCMA and MCMA and studying the corresponding confusion matrices, it is possible to assert that in general the highest percentages in the confusion matrices occur with elements (CC, CC), (CNC, PC), (CNC, PNC), and (CNC, CNC) and the lowest ones are associated with (PC, CNC), (CC, CNC), (PC, PNC), and (PNC, CNC), where the first and the second elements in the previous couples refer to MCMA and DTCMA, respectively. Almost all of the pixels classified as CC by MCMA are classified as CC by DTCMA, almost all of the pixels classified as PC by MCMA are classified as PC or CC by DTCMA, and the majority of the pixels classified as PNC and CNC by MCMA are both classified as PC by DTCMA. The majority of the pixels classified as CC by DTCMA are also classified as CC by MCMA; the majority of the pixels classified as PC and almost all of the pixels classified as PNC and CNC by DTCMA are all classified as CNC by MCMA.

Each MCMA test t is characterized by a high-confidence cloudy-sky threshold value α_t and a high-confidence clear-sky value β_t, and MCMA labels a scene pixel as CC, PC, PNC, or CNC depending on the

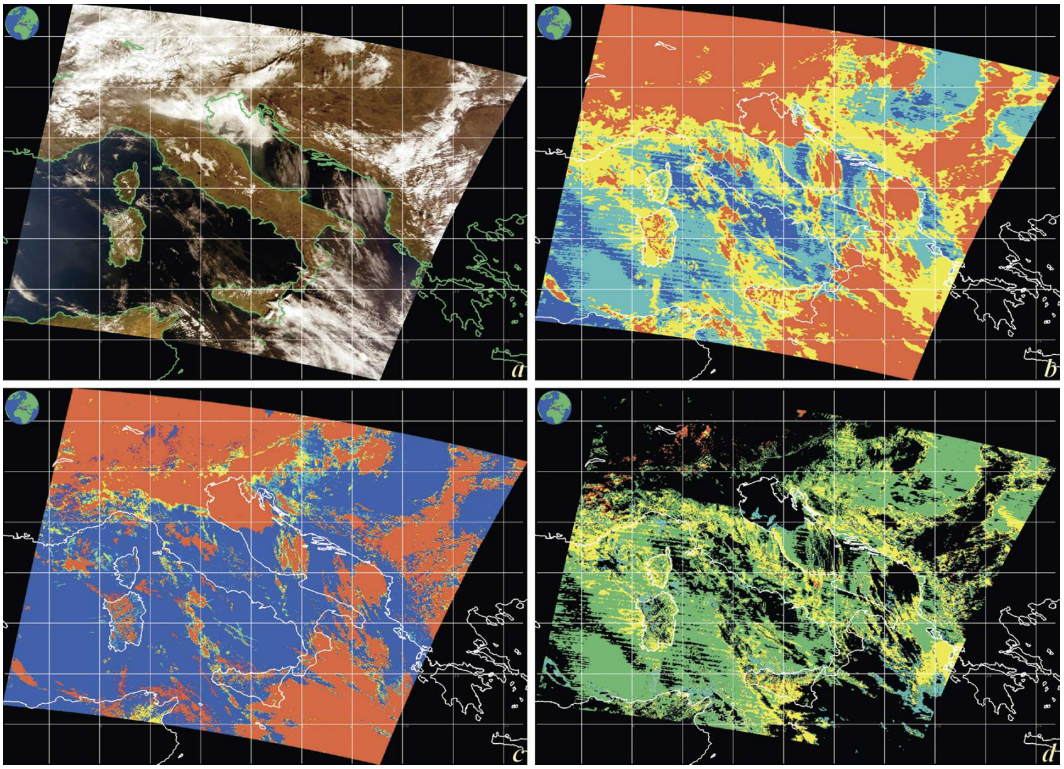

FIG. 8. (a) Visible-spectrum, (b) DTCM, (c) MCM, and (d) DTCM − MCM images for 11 Feb 2002.

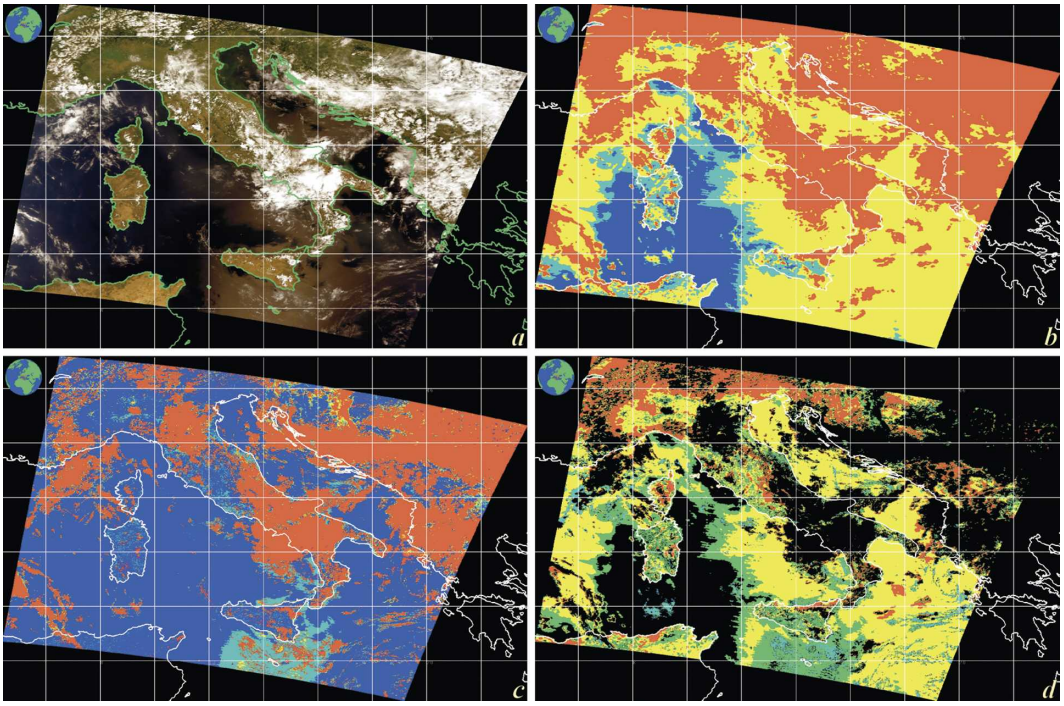

FIG. 9. (a) Visible-band, (b) DTCM, (c) MCM, and (d) DTCM − MCM images for 30 Jul 2002.

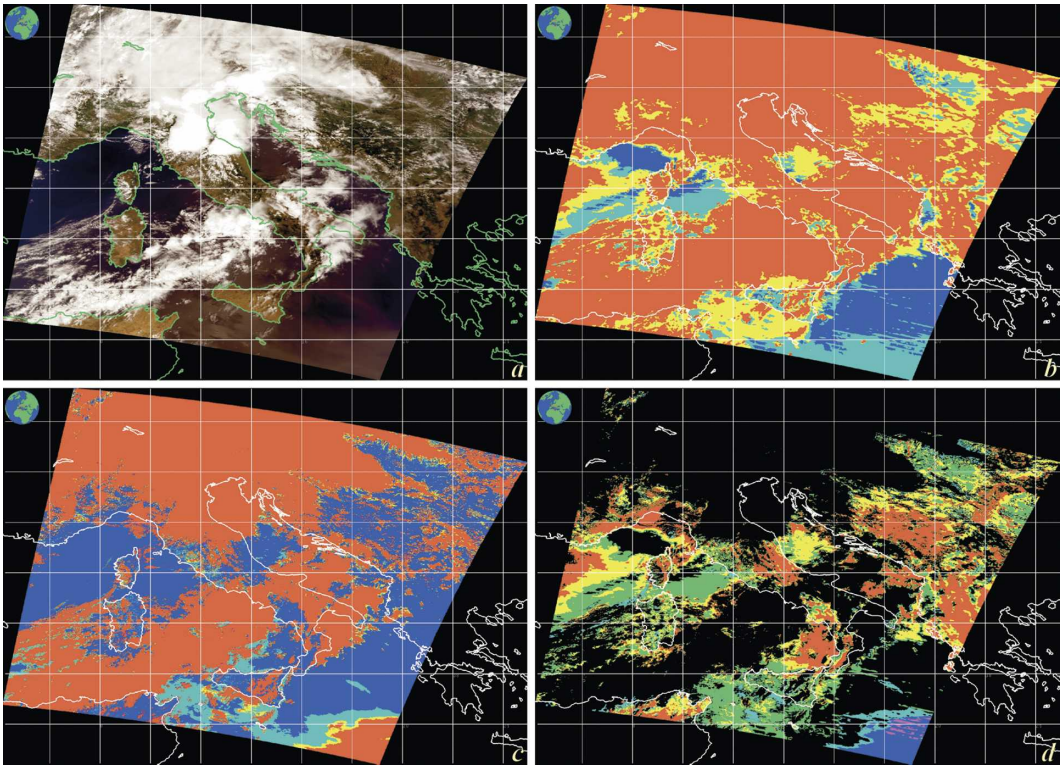

FIG. 10. Same as Fig. 9, but for 6 Aug 2002.

pixel value position in comparison with α_t and β_t (section 2). The values of α_t and β_t are determined from a large number of observations and theoretical simulations. Each observed radiance value Z_t is compared with its corresponding clear-sky radiance value β_t, and, if it is altered by more than the uncertainty $u(\beta_t)$ in the clear-sky values, clouds are detected. In this way the threshold α_t for cloud detection is the arithmetic sum of the clear-sky radiance mean value β_t and the magnitude $u(\beta_t)$ of the uncertainty in the clear-sky radiance estimate [$\alpha_t = \beta_t \pm u(\beta_t)$]. A pixel is classified as cloudy only if at least one radiance value Z_t is distinct from the inferred clear-sky radiance mean value β_t by an amount larger than the uncertainty $u(\beta_t)$. This last quantity can be caused both by measurement errors and by natural variability and is a function of the instrument noise in that channel and the magnitude of the correction that was necessary because of surface spectral radiative properties, as well as atmospheric moisture and aerosol reflection contributions (Ackerman et al. 2002).

DTCMA is characterized by a set of nine end members ($\mathbf{E}_1$, $\mathbf{E}_2$, . . . , $\mathbf{E}_9$) and a set of nine spectral angles (Ω_1, Ω_2, . . . , Ω_9). If a scene pixel lies within the seven-dimensional cone determined by the end member $\mathbf{E}_t$ and the spectral angle Ω_t (point 2 of section 3), it is considered to be a test-t typical cloudy pixel (t = 1, 2, . . . , 7); if the scene pixel lies within the seven-dimensional cone determined by the end member $\mathbf{E}_8$ and the spectral angle Ω_8 (point 6 of section 3), it is considered to be a typical land clear-sky pixel; if the scene pixel lies within the cone determined by $\mathbf{E}_9$ and Ω_9 (point 6 of section 3), it is considered to be a typical sea clear-sky pixel. All of the pixels that satisfy these conditions are used to calculate the averages mcl_t, mcs_t, mncl_t, and mncs_t, which correspond to α_t and β_t of MCMA for every test t [points 3, 7, and 8 and Eq. (1) of section 3].

The aim of this work is to compare the cloud masks obtained by MCMA, which uses thresholds α_t and β_t determined in advance for several environmental and temporal domains (Ackerman et al. 2002), with the results retrieved by using the end members $\mathbf{E}_1$, $\mathbf{E}_2$, . . . , $\mathbf{E}_9$ and the spectral angles Ω_1, Ω_2, . . . , Ω_9.

TABLE 15. Confusion matrix for 11 Feb 2002.

	CC MCM	PC MCM	PNC MCM	CNC MCM
CC DTCM	31.5	2.5	0.5	0.9
PC DTCM	4.0	4.0	4.3	17.5
PNC DTCM	0.0	0.1	0.2	25.1
CNC DTCM	0.0	0.0	0.1	9.3

TABLE 16. Confusion matrix for 30 Jul 2002.

	CC MCM	PC MCM	PNC MCM	CNC MCM
CC DTCM	27.6	2.7	1.4	8.4
PC DTCM	2.6	1.6	6.1	29.7
PNC DTCM	0.1	0.0	0.4	7.1
CNC DTCM	0.0	0.0	0.0	12.2

TABLE 17. Confusion matrix for 6 Aug 2002.

	CC MCM	PC MCM	PNC MCM	CNC MCM
CC DTCM	54.5	2.4	1.5	10.1
PC DTCM	1.9	1.6	3.5	10.0
PNC DTCM	0.9	0.3	1.3	6.0
CNC DTCM	0.1	0.0	0.4	5.5

Even though

1) DTCMA is a MCMA simplification, because it applies only a subset of all the MCMA tests (Ackerman et al. 2002);
2) MCMA performs even clear-sky restoral tests, which are invoked during daylight hours in areas where land and water surfaces coexist (as almost everywhere in the south of Italy), in regions identified as shallow water (as in many places along the Italian coastline), and in areas affected by sunglint (this phenomenon takes place often in the south of Italy, an area that has a large amount of sunshine) (Ackerman et al. 2002) and which make DTCMA cloud masks generally cloudier than MCMA ones;
3) MCMA uses many data inputs that DTCMA does not, such as the azimuthal and viewing angles, the elevation above mean sea level, the map of ecosystems, the daily snow/ice map, and the daily ice concentration (Ackerman et al. 2002);
4) MCMA also adopts destriping methods; and
5) the end members and the spectral angles determined and used in this work are not supported by sizeable statistics and thus their asymptotic orientations were not achieved;

the cloud masks retrieved with DTCMA satisfactorily match the MCMA ones; thus the possibility that the usage of end members and spectral angles instead of the MCMA thresholds might be easier or might provide higher regional-scale performances must be carefully examined.

5. Further developments

The achieved results make it understood that the following three problems must be faced: the periodic noise affecting the cloud masks obtained by DTCMA, the extension of the training statistics and the validation of DTCMA cloud masks.

Image striping may be caused by the coupling of periodic signals related to the raster scan and data-sampling mechanism into the imaging electronics of electro-optical scanners or by power consumption

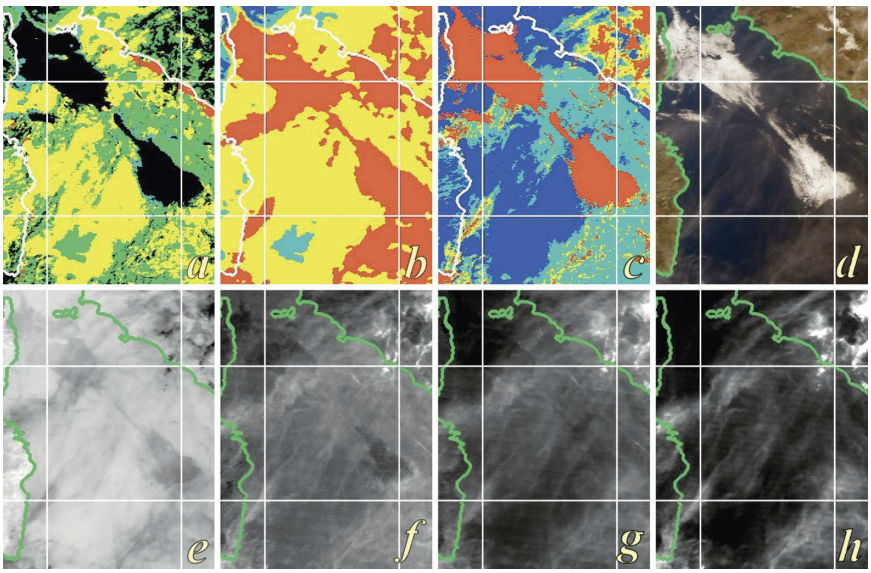

FIG. 11. Images of (a) DTCM − MCM, (b) DTCM, (c) MCM, (d) visible-band scene, (e) $\mathbf{Z}_1$, (f) $\mathbf{Z}_2$, (g) $\mathbf{Z}_3$, and (h) $\mathbf{Z}_6$ for 28 Jan 2002.

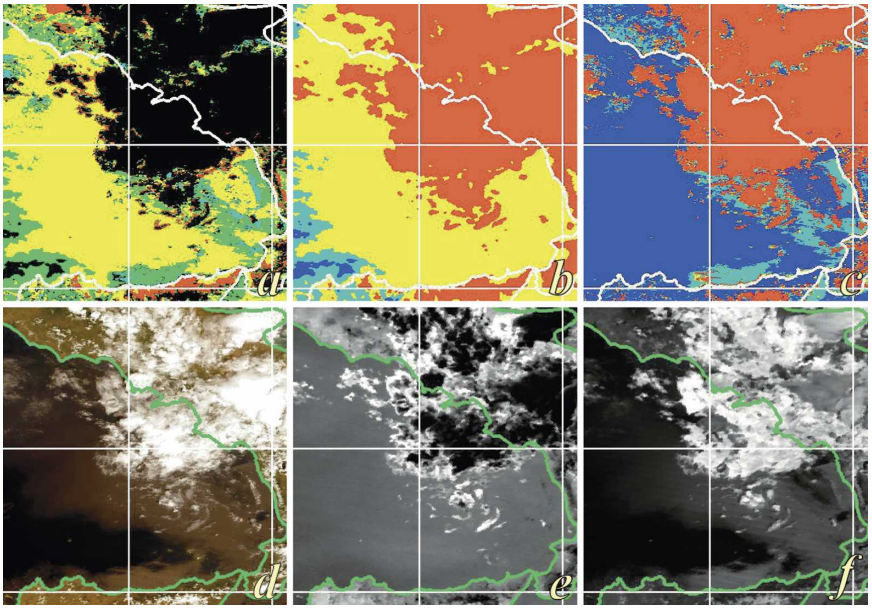

FIG. 12. Images of (a) DTCM − MCM, (b) DTCM, (c) MCM, (d) visible-spectrum scene, (e) $\mathbf{Z}_2$, and (f) $\mathbf{Z}_4$ for 30 Jul 2002.

variations and mechanical oscillations in electromechanical scanners or tape recorders (Moik 1980). Periodic noise can be removed by Fourier methods, but a simple bandwise Fourier filtering may corrupt significant parts of the relevant signal (Moik 1980; Nielsen 1999). Therefore, we should minimize the amount of filtering by skipping or filtering the MNF bands that contain the noise in question before transforming back from MNF space to the original image domain (Nielsen 1999). Regular striping in MODIS images occurs because data are taken by a multidetector sensor and the transfer functions of the individual detectors are not identical, because of temperature variations and changes in detector materials (Moik 1980). Cloud-mask striping could be removed by making each detector subimage possess the same mean and variance of the full image (Moik 1980) or even by matching the empirical distribution functions of the subimages obtained by collecting the scan lines of each sensor detector (Weinreb et al. 1989).

The statistics concerning the training step will be extended to the other two seasons of the year. In this way it will be possible to study the evolution of the end members according to the various seasons and to verify whether the end members $\mathbf{E}_r$ with $r = 1, 2, \ldots, 7$ can be considered regardless of the month of the year. The results of this analysis will integrate the algorithm and will allow it to produce cloud masks for every month of the year. After that the algorithm will be applied to MSG images.

Last, the problem of the validation of the results will be faced. To this purpose cloud masks of MODIS (MOD35_L2 products) and of other sensors, such as Meteosat, will be used. Also, data from aircraft, balloon, and ground platforms may be acquired. Among ground-based systems, lidar (Di Girolamo et al. 1994) gives interesting performances for validation purposes (Ackerman et al. 2002).

Acknowledgments. This work has been carried out within the framework of the Nowcasting Research Program funded by the Italian Minister of Research and University under the Cluster II program.

REFERENCES

Ackerman, S. A., K. I. Strabala, W. P. Menzel, R. A. Prey, C. C. Moeller, and L. E. Gumley, 1998: Discriminating clear-sky from clouds with MODIS. *J. Geophys. Res.,* **103,** 32 141–32 157.

——, and Coauthors, 2002: Discriminating clear-sky from clouds with MODIS. Algorithm Theoretical Basis Doc. MOD35, ATBD-MOD-06, 115 pp.

Ball, G. H., and J. D. Hall, 1967: A clustering technique for summarizing multivariate data. *Behav. Sci.,* **12,** 153–155.

Di Girolamo, P., V. Cuomo, G. Pappalardo, R. Velotta, and V. Berardi, 1994: Lidar validation of temperature and water vapor satellite measurements. *Lidar Techniques for Remote Sensing,* C. Werner, Ed., International Society for Optical Engineering (SPIE Proceedings Vol. 2310), 71–83.

Dowdy, S., and S. Wearden, 1991: Inference about two variances. *Statistics for Research,* 2d ed. John Wiley and Sons, 213–216.

ENVI User's Guide Team, 2003: *ENVI User's Guide.* Research Systems, Inc., 1084 pp.

Gao, B. C., P. Yang, W. Han, R. R. Li, and W. J. Wiscombe, 2002: An algorithm using visible and 1.38 μm channels to retrieve cirrus cloud reflectances from aircraft and satellite data. *IEEE Trans. Geosci. Remote Sens.,* **40,** 1659–1668.

Green, A. A., M. Berman, P. Switzer, and M. D. Craig, 1988: A transformation for ordering multispectral data in terms of image quality with implications for noise removal. *IEEE Trans. Geosci. Remote Sens.,* **26,** 65–74.

Justice, C., and Coauthors, 1998: The Moderate Resolution Imaging Spectroradiometer (MODIS): Land remote sensing for global change research. *IEEE Trans. Geosci. Remote Sens.,* **36,** 1228–1249.

King, M. D., Y. Kaufman, W. Menzel, and D. Tanr, 1992: Remote sensing of cloud, aerosol, and water vapor properties from the Moderate Resolution Imaging Spectrometer (MODIS). *IEEE Trans. Geosci. Remote Sens.,* **30,** 2–27.

Kruse, F. A., A. B. Lefkoff, J. B. Boardman, K. B. Heidebrecht, A. T. Shapiro, P. J. Barloon, and A. F. H. Goetz, 1993: The Spectral Image Processing System (SIPS), interactive visualization and analysis of imaging spectrometer data. *Remote Sens. Environ.,* **44,** 145–163.

Moik, J. G., 1980: *Digital Processing of Remotely Sensed Images.* U.S. Government Printing Office, 330 pp.

Nielsen, A. A., 1999: Orthogonal Transformations, C04351 Statistical Image Analysis, Lecture Notes, Technical University of Denmark, 13 pp. [Available online at http://www2.imm.dtu.dk/pubdb/views/edoc_download.php/3088/pdf/imm3088.pdf.]

Schmetz, J., H. Woick, S. A. Tjemkes, and M. Rattenborg, 1998: From Meteosat to Meteosat Second Generation (MSG). Preprints, *Ninth Conf. on Satellite Meteorology and Oceanography,* Paris, France, Amer. Meteor. Soc., 335–338.

Watts, P. D., C. T. Mutlow, A. J. Baran, and A. M. Zavody, 1998: Study on cloud properties derived from Meteosat Second Generation observations. EUMETSAT ITT Final Rep. 97/181, 344 pp.

Weinreb, M. R., R. Xie, J. H. Lienesch, and D. S. Crosby, 1989: Destriping GOES images by matching empirical distribution functions. *Remote Sens. Environ.,* **29,** 185–195.

Woick, H., J. Schmetz, and S. A. Tjemkes, 1997: An introduction to Meteosat Second Generation imagery and products. *Proc. 1997 EUMETSAT Meteorological Satellite Data Users' Conf.,* Brussels, Belgium, EUMETSAT, 395–400.